

Lawrence Berkeley National Laboratory

LBL Publications

Title

Fabrication of single crystal architecture in Sb-S-I glass: Transition from dot to line

Permalink

<https://escholarship.org/uc/item/28g8g1mt>

Authors

Savytskii, Dmytro
Dierolf, Volkmar
Tamura, Nobumichi
et al.

Publication Date

2018-12-01

DOI

10.1016/j.jnoncrysol.2017.12.007

Peer reviewed



Contents lists available at ScienceDirect

Journal of Non-Crystalline Solids

journal homepage: www.elsevier.com/locate/jnoncrysol

Fabrication of single crystal architecture in Sb-S-I glass: Transition from dot to line

Dmytro Savytskii^a, Volkmar Dierolf^b, Nobumichi Tamura^c, Himanshu Jain^{a,*}^a Materials Science and Engineering Department, Lehigh University, 5 East Packer Avenue, Bethlehem, PA 18015, USA^b Physics Department, Lehigh University, 16 Memorial Drive East, Bethlehem, PA 18015, USA^c Lawrence Berkeley National Laboratory, Berkeley, CA 94720, USA

ARTICLE INFO

Keywords:

Single crystals
Glasses
Laser
Crystallization
Nucleation
Growth

ABSTRACT

We have investigated the occurrence of the sometimes observed grain boundaries, as initial seed is extended to form line in laser-fabricated single-crystal architecture in glass (SCAG). In particular, for Sb_2S_3 SCAG in Sb-S-I glass as a model system, grain boundaries are formed during the transition from laser-written initial seed dot to crystal line. Such grain boundaries during the growth of Sb_2S_3 crystals occur in $16\text{SbI}_3\text{--}84\text{Sb}_2\text{S}_3$ glass, whereas they are absent in Sb_2S_3 glass. We correlate this difference in tendency to form multiple grains with the relative glass forming ability i.e. the dynamics of nucleation and crystal growth as determined by differential scanning calorimetry (DSC). On the basis of this understanding, methods to minimize the appearance of grain boundaries in the transition region are suggested.

1. Introduction

Laser-induced crystallization of glass has become a viable method for fabricating single crystals, where a laser is used to heat the glass locally to initiate nucleation and form a seed crystal, which is then grown into a single crystal line. A continuous wave (CW) laser is used to create single-crystal architecture in glass (SCAG) at or near the surface, whereas femtosecond (fs) laser can yield SCAG in 3D deep inside the glass [1–9]. Recently, we reported the fabrication of Sb_2S_3 single crystal dots (0D), lines (1D) and 2D structures [6–8] on the surface of Sb-S-I glasses by heating the glass from ambient to crystallization temperature (T_x) without melting. The amorphous phase was directly converted into a single crystal by solid-solid transformation via space selective continuous wave (CW) laser heating of glass [9]. This glass crystallizes into a ferroelectric phase [10], making the study interesting both for scientific understanding and technological applications. Sb_2S_3 is a promising material for photovoltaic cells since it shows high absorption coefficient ($\alpha > 10^3 \text{ cm}^{-1}$), and its band gap (1.6–2.5 eV) covers the maximum span of the visible and near infrared ranges of the solar spectrum [11]. In addition, Sb_2S_3 has attracted attention for its applications in thermoelectric [12] and optoelectronic [13] devices in the IR region.

Fabrication of Sb_2S_3 crystals was initiated with the formation of a seed crystal nucleated at or just below the surface of glass with laser beam exposure for 65 s. Sample was then moved in a straight line at a

typical speed of $20 \mu\text{m/s}$ while the laser position remained fixed, resulting in linear 1D crystal lines [6,9]. Heating with a focused laser beam with diameter $3\text{--}4 \mu\text{m}$ limits the volume of glass so that within this region effectively one viable nucleus is allowed to form, which then is induced to grow quickly first into a single crystal dot. Unwanted additional nucleation is avoided by moving the laser beam at a sufficiently fast rate such that there is no time for forming extraneous crystals [9].

Often the single crystal lines fabricated by laser-induced solid-solid transformation display orientational changes, as observed for laser-induced Sb_2S_3 crystals laser-formed on the surface of Sb-S-I glasses [6–9]; it has been observed also within individual grains of isothermally formed glass-ceramic [14–16]. In such a crystal, the lattice orientation may vary systematically in a well-defined manner. For the single crystal lines of Sb_2S_3 , electron backscatter diffraction (EBSD) mapping indicated gradually rotating crystal lattice about a direction parallel to glass surface and normal to growth direction (which is sometimes equivalent to the laser scanning direction). Scanning X-ray micro-diffraction (μSXRD) Laue patterns showed split spots surrounded by narrow streaks along the laser scanning direction, similar to the observation of plastic deformation in nano-indented pure metal single crystals. We therefore concluded that laser-grown Sb_2S_3 single crystal contains unpaired dislocations and small-angle tilt boundaries, which are responsible for the observed lattice rotation [6].

The dot initially created on glass, which serves as a seed for a line,

* Corresponding author at: Department of Materials Science and Engineering, Lehigh University, 5 East Packer Avenue, Bethlehem, PA 18015, USA.
E-mail address: h.jain@lehigh.edu (H. Jain).

<https://doi.org/10.1016/j.jnoncrysol.2017.12.007>

Received 29 September 2017; Received in revised form 1 December 2017; Accepted 3 December 2017
0022-3093/© 2017 Elsevier B.V. All rights reserved.

shows a more complicated radial character of lattice rotation and broader Laue reflections than for a line [6]. The different character of dislocation structure in the seed region (dot) and along the line is likely to be caused by the different heat profile of corresponding stationary and moving laser spot, which determines the direction and shape of crystal growth front. When the initial dot is formed, both the heat profile and corresponding crystallization front have circular shape, in contrast to what is observed for a moving spot in one particular (scanning) direction during the formation of crystal line where the position of the front changes dynamically.

Whereas the nature of lattice rotation in an isolated dot and line appear to be understood reasonably well, the region of transition from dot to line is much more complex and remains to be analyzed. For example, in contrast to gradual rotation of crystal lattice observed in the dots and lines consisting of dislocation and small angle grain boundaries, in the transition region we found large angle grain boundaries which sometimes originated at the edge of the crystal dots with a jump in crystal orientation leading into the line. In this paper, we investigate the origin and nature of such boundaries. Then methods are explored to eliminate these defects that are introduced at the beginning of crystal line fabrication.

2. Experimental

Two types of glasses were used: congruently crystallizing Sb_2S_3 and non-stoichiometric $16\text{SbI}_3\text{--}84\text{Sb}_2\text{S}_3$. They were prepared by the melt-quench method, as described previously [6]. For both compositions the resulting crystal is stoichiometric Sb_2S_3 . As a result, for the latter glass the crystal growth process is additionally complicated by the long range diffusion of species, because the composition of the crystal and glass matrix is different.

Differential scanning calorimetry (DSC) was used for identifying the thermal characteristics of glass-crystal transformation. Specifically, the glass transition (T_g) and maximum crystallization (T_c) temperatures were determined with a DSC system (model Q2910, TA Instruments, New Castle, DE, USA). Samples of the two glass compositions with a particle size of 0.5–0.7 mm were tested at the heating rate of 15 K/min from ambient to 300 °C.

Absorption spectroscopy revealed that the optical band-gap of the synthesized glasses and Sb_2S_3 crystals is different with values 2.1 and 1.7 eV, respectively [17,18]. To cause absorption of the laser beam enough for heating of glasses but relatively small by crystal, we selected a CW diode laser with intermediate wavelength of 639 nm (i.e. 1.94 eV).

Crystalline dots were created from glass by slowly ramping the power density of laser from 0 to $90 \mu\text{W}/\mu\text{m}^2$ within a 5 s period. Upon reaching the final power ($90 \mu\text{W}/\mu\text{m}^2$), the laser was held in place at the same position for an additional duration, typically 60 s. The crystal lines were fabricated by translating the sample (after the initial crystallization of dot) while maintaining the power density. For this study, a 639 nm ThorLabs LP639-SF70 single mode fiber pigtailed laser diode was employed. This laser provided the ability to precisely control the intensity using ILX Lightwave LDX-3545 Precision Current Source with an analog control input. Using a microscope objective (numerical aperture 0.75) illuminated spots of 3–4 μm diameter were produced on the polished surface of the glass sample. The sample rested on a custom-built stage which allowed the control of the pitch and tilt of the surface, as well as motorized translation in the x-, y-, and z-directions. A small enclosure around the sample was fabricated through which nitrogen gas flowed at a low rate. This arrangement allowed the irradiation to take place in an environment effectively free of oxygen. Finally, a white light source illuminated the sample and a CCD camera provided in-situ monitoring of the sample. A LabView software controlled the positioning and movement of the stage, as well as the laser intensity. The optical setup and procedures for the preparation of the glass samples and fabrication of crystals have been described in detail in previous

publications [19,20].

The laser-irradiated regions were analyzed with a Scanning Electron Microscope (SEM, Hitachi 4300 SE) in water vapor environment to minimize the charging effects. Crystallinity and orientation of the crystal grains in laser created patterns were examined by EBSD, in which Kikuchi patterns were collected by a Hikari detector inserted into the specimen chamber. The crystalline grains and their orientation were determined through EBSD mapping scans. The step size for these maps was 0.2 μm with a hexagonal sampling grid. The collected scans were indexed by TSL (TexSEM Laboratory) orientation data collection and analysis software using Sb_2S_3 crystal structure reference parameters. Indexing of diffraction patterns was achieved by a voting system and characterized by a number of parameters such as the image quality (IQ) value votes, the fit-factor, and the confidence index (CI). The orientation imaging microscopy (OIM) software package was used to identify crystal grains and generate image quality, phase, and inverse as well as direct pole figure maps. For our EBSD mapping experiment the samples were positioned in such way that the scanning direction of the laser corresponded to the rolling direction (RD) in specific EBSD setting. Using the TSL software, the inverse pole figure (IPF) maps were also obtained for the normal (ND) direction. Each IPF map indicates the lattice orientation along the direction of a reference axis. We consider three orthogonal reference axes in order to determine the orientation of the crystal. The RD-map gives the orientation parallel to the line itself, the ND-map gives the orientation in the direction normal to the surface, and the TD-map gives the orientation orthogonal to both. All the maps were corrected by removing points with low CI values associated with amorphous region or cracks, grain boundaries, and surface defects.

The crystallinity and orientation of the laser created dots and lines were further examined by μSXRD with micrometer spatial resolution on beamline 12.3.2 of the Advance Light Source synchrotron, Lawrence Berkeley National Laboratory [21]. Polychromatic x-ray beam with an energy range of 6–22 keV was focused to a micron size via a pair of elliptically bent x-ray mirrors in a Kirkpatrick-Baez configurations. Samples were raster scanned under the x-ray beam with a step size of 1 μm in 45° inclined configuration relative to incoming white X-ray beam and detector with the crystal lines oriented along the beam. At each step a Laue pattern was collected using a DECTRIS Pilatus 1 M hybrid pixel detector with exposure time of 1–2 s. Indexing of the Laue patterns was completed using the XMAS software [22].

3. Results and discussion

The panels of Fig. 1 describe the nature of the so formed crystal imaged in (a) by SEM, which is established from a detailed analysis of the lattice orientation by EBSD mapping. Fig. 1(b) presents an image quality (IQ) color map of the selected region. Correspondingly, blue and green points in the IQ map for the area around the laser-induced protrusion region have low (< 200) IQ-values, which indicate amorphous state. In contrast, for the majority of the laser irradiated region (dot and line) the IQ values are much higher indicating the presence of crystal-line phase. However, IQ-values are relatively low also in the upper half of the dot region, which is a result of surface roughness evident in Fig. 1(a). As it was shown in previous works [23,24], under laser irradiation of $16\text{SbI}_3\text{--}84\text{Sb}_2\text{S}_3$ for long times (> 0.5 min) SbI_3 evaporates, which produces strong surface erosion and explains the observed crater-like morphology of the dot. The evaporation of the SbI_3 enriches the remaining supercooled liquid with Sb_2S_3 , which stimulates nucleation and further crystal growth of this phase in the dot. For short exposure times, such as in the linear region, the change in composition occurs via a uniform diffusion process.

Fig. 1(c) and (d) show the inverse pole figure (IPF) and crystal orientation deviation (COD) maps, which indicate that in the dot region a single crystal of Sb_2S_3 was produced in a shape of ellipse by laser writing. The blue colored pixels indicate close to <110>-orientation of the grain in the direction normal to the sample surface. Remarkably, the

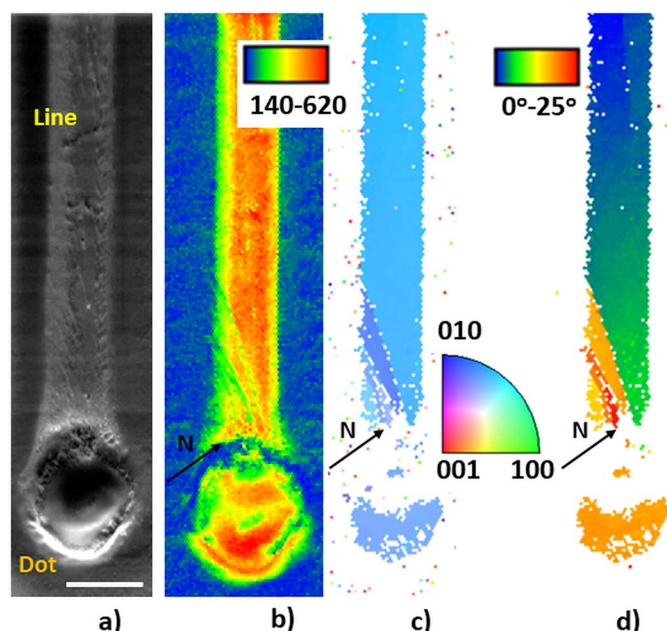


Fig. 1. Sb_2S_3 SCAG consisting of initial dot and subsequent line on the surface of $16\text{SbI}_3\text{-}84\text{Sb}_2\text{S}_3$ glass: SEM image (a), image quality (IQ) (b), colored inverse pole figure (IPF) map with reference vector normal to sample surface (ND) (c) and crystal orientation deviation (COD) map (d). The crystal dot was created by slowly ramping in 5 s the power density from 0 to $90 \mu\text{W}/\mu\text{m}^2$ and then constant power exposure for 60 s. It was subsequently transformed to a crystal line by moving the laser spot at a scanning speed $20 \mu\text{m}/\text{s}$ in nitrogen environment for a distance of $75 \mu\text{m}$. Scale bar corresponds to $5 \mu\text{m}$.

Sb_2S_3 single crystal of the dot changed its orientation at the beginning of the line, forming a few grains with orientation intermediate between that of the preceding dot and succeeding line. Low IQ-values were observed in the regions of grains boundaries on the map in Fig. 1(b). At the beginning of the line the COD map, which can discern small misorientations and low-angle grain boundaries, shows three grains separated by large angle boundaries, which later disappear and only one single grain grows in the line.

In the region of dot both the IPF and COD orientation maps visually exhibit a single uniform color (Fig. 1(c) and (d)), which indicate the single crystal nature of the dot. To further elucidate the appearance of grains and their structure in the top half of the dot, we exploited μSXRD for a more precise orientation mapping of crystal architecture with $\sim 1 \mu\text{m}$ spatial resolution [21]. In contrast to EBSD, which gives information about surface layer with thickness of few tens of nanometers and have poor angle resolution ($1^\circ\text{--}2^\circ$), the ultra-bright X-ray beam is able to penetrate materials for a distance greater than one hundred microns and can detect crystal grains with misorientation ($\sim 0.1^\circ$) one order of magnitude smaller than by the EBSD technique.

Fig. 2 shows morphology of dot and crystal as seen by SEM together with a detailed analysis of crystal lattice orientation by μSXRD . An important observation is that the morphological variation seen in the SEM image (Fig. 2(a)) does not affect lattice orientation that is established unambiguously by μSXRD . The Laue diffraction patterns for two different points of the crystal (shown in Fig. 1) – one within the dot and another in the line are shown in Fig. 2(b). Enlarged images of a selected (12,14,2) reflection from the former show some broadening (bottom image on Fig. 2(c)) in comparison to what is expected from an ideal single crystal. This deviation suggests that some distortion of the crystal lattice occurs within the scattering volume in the dot. The image of a Laue spot, obtained from the line (top image on Fig. 2(c)), comprises of reflections with additional scattering indicated by narrow streaks elongated along the laser scanning direction.

Further details of the spatial orientation of local lattice of the crystal architecture are obtained from pole figure maps (Fig. 2(d)). The IPF

map in Fig. 1(c) established that the crystallographic direction [110] is practically normal to the surface of the sample and therefore it is well suited for assessing the variation of crystal orientation in space. Thus the pole figure map for [110] in Fig. 2(d) clearly expresses lattice rotation within the line. On this pole figure map the points that correspond to the line form a practically straight segment, length of which in angular space equals 8.4° . It means that for the selected line length of $35 \mu\text{m}$ the crystal is rotated at an average rate of $\Theta \sim 0.24^\circ/\mu\text{m}$. As mentioned in Introduction, unpaired dislocations and small-angle tilt boundaries are responsible for the observed lattice rotation [6]. The fundamental reason for the presence of such dislocation/disclination structure is the difference in the structure of the crystalline phase and precursor glass. During the solid to solid transformation of glass into a crystal under laser heating such as employed here, there is a concomitant decrease in volume [6]. Such a change should place the crystal under tension and the surrounding glass under compression. Then the easiest way for the crystal to absorb the tension is via formation of misfit dislocations.

The beginning of the line is misoriented by $\sim 5.4^\circ$ relative to the overall dot region. From the pole figure map we find that the dot is not a single crystal, but consists of two large fragmentations misoriented from each other by $\sim 0.5^\circ$, which are further divided in a few tens of nanograins misoriented by $< 0.05^\circ$ relative to each other (bottom image on Fig. 2(d)). If we combine together these two large parts – in other words, if we neglect angular gap 0.5° between them, then we receive a figure close to weakly distorted ellipse that corresponds to the shape of the dot. These results confirm what we discovered previously for 1D lines [6]: the direction of lattice rotation is specified by the growth direction. For the dot a nucleus appear in the dot center and then a crystal grows radially forming hemisphere if we assume isotropy of crystal growth. That is, the crystal grows radially and its lattice also rotates radially [8].

The EBSD and μSXRD results of other lines (see also Fig. S1 in Supplementary information) show that Sb_2S_3 single crystals induced by laser beam on the surface of $16\text{SbI}_3\text{-}84\text{Sb}_2\text{S}_3$ glass sometimes abruptly change their orientation as the dot transitions to line, such as marked by arrow with letter N in Fig. 1. However, no such “intermediate” grains were observed when the same procedure was followed on the surface of stoichiometric Sb_2S_3 glass and the transition of Sb_2S_3 crystal from dot to line was analyzed. We should note that in the case of $16\text{SbI}_3\text{-}84\text{Sb}_2\text{S}_3$ glass, due to the SbI_3 component, the chemical composition of the surrounding of Sb_2S_3 both - crystalline line as well as dot - would be changed. But, grains were observed only in transition region between a dot and a line. Naturally, one question arises: why is crystal growth at the beginning of lines so different for the two glasses investigated here? To explain such difference in laser-crystallization behavior we need to take into account that Sb_2S_3 glass could be synthesized only at very fast cooling rates and its composition falls outside the nominal glass forming region [23,25]. In contrast, the $16\text{SbI}_3\text{-}84\text{Sb}_2\text{S}_3$ composition corresponds to glass forming region, so the glass could be fabricated at a comparatively low cooling rate. Our DSC measurements presented in Fig. 3 also show that the thermal stability and tendency for crystallization of these two glasses differ greatly. The DSC scan of $16\text{SbI}_3\text{-}84\text{Sb}_2\text{S}_3$ shows glass transition at 190°C , and its crystallization to Sb_2S_3 phase, as shown by the exothermal peak, begins at 245°C . For Sb_2S_3 composition the glass transition is hardly detectable by DSC due to the strong overlapping of glass transition and crystallization of Sb_2S_3 phase.

Using the general knowledge of crystallization process [26] we have schematically plotted temperature dependences of the crystal nucleation and growth rates for both glass compositions in Fig. 4. Here we have made use of the fact that the $16\text{SbI}_3\text{-}84\text{Sb}_2\text{S}_3$ (Fig. 4(a)) glass composition is within, while Sb_2S_3 (Fig. 4(b)) composition is outside the nominal glass-forming region [23,25]. For both cases we can select two temperature ranges: S, where both the nucleation and crystal growth rate curves overlap, and P, where only nucleation is possible. For glass-

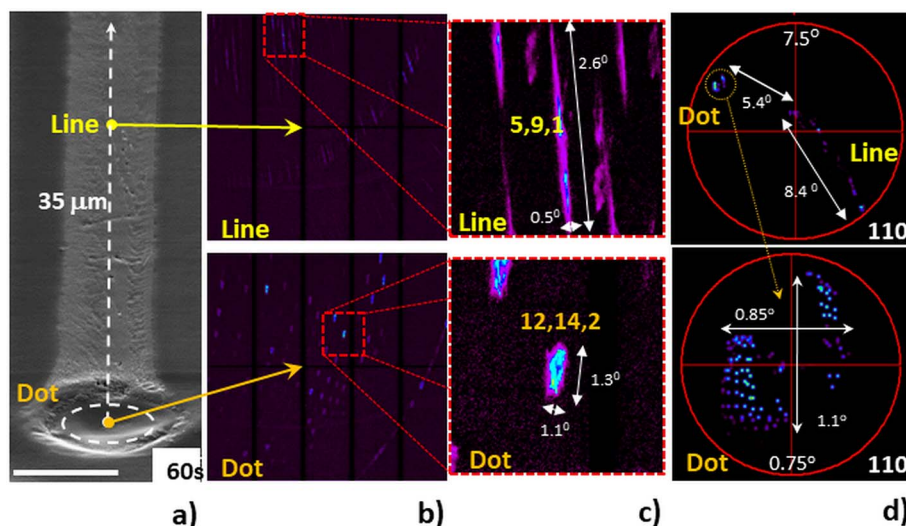


Fig. 2. Results of scanning X-ray microdiffraction (μ SXRD) of Sb_2S_3 crystal architecture shown in Fig. 1. SEM image (a) and Laue diffraction patterns (b) collected from the dot (bottom) and the line (top). Magnified images (c) of selected reflection (12,14,2) and (5,9,1) extracted from corresponding Laue patterns (b) obtained for different points of the crystal (a). Pole figure map for [110] crystallographic direction of the crystal architecture (d, top) calculated from μ SXRD data. The magnified pole figure map (d, bottom) corresponds to the dot of the crystal architecture.

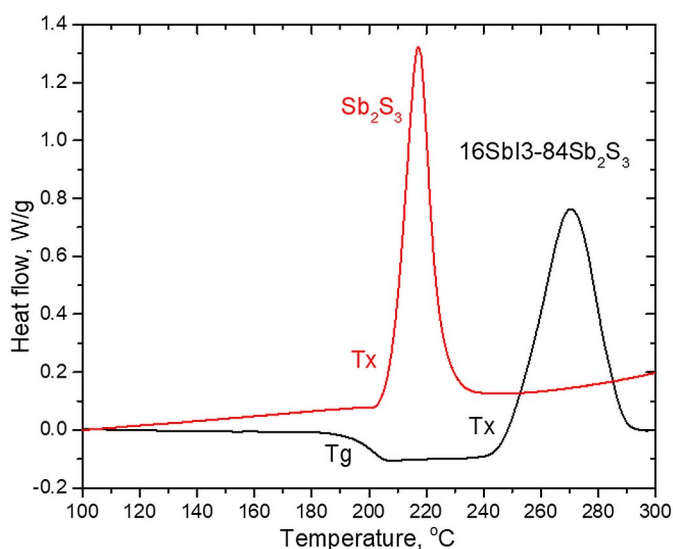


Fig. 3. DSC data for Sb_2S_3 (red line) and $16\text{SbI}_3\text{-}84\text{Sb}_2\text{S}_3$ (black line) glasses collected at 15 K/min heating rate. (For interpretation of the references to color in this figure legend, the reader is referred to the web version of this article.)

forming composition ($16\text{SbI}_3\text{-}84\text{Sb}_2\text{S}_3$) the P range is wider than for non-glass-forming glasses, for example, Sb_2S_3 . Assuming that nucleation process starts mainly in supercooled state (which is above T_g), and using DSC data (Fig. 3) we may conclude that the P range is close to zero for non-glass-forming Sb_2S_3 sample and reaches 55 K for $16\text{SbI}_3\text{-}84\text{Sb}_2\text{S}_3$ glass.

If we consider laser-induced crystallization by heating of the sample from room temperature to T_x , then for CW laser induced temperature field also we have two S and P temperature zones (Fig. 4(c) and (d)). Zone S , which is localized in the center of the spot, corresponds to the area where we can grow single crystal, because the first nucleus which appears in this zone has the possibility to grow and cover all this central region of the laser spot. The temperature of nucleation onset (T_n) is always lower than T_x [27,28]. Zone P , which corresponds to the region where unwanted nuclei are likely to form and remain stable around the S zone is shown schematically in Fig. 4(c) and (d). The difference between glass-forming and non-glass-forming cases is the width of the P zone. For non-glass-forming compositions it is close to zero and therefore not shown in Fig. 4(d), in contrast to glass-forming case (Fig. 4(c)), where it is ~ 55 K of temperature range and can reach few microns around the central single crystal in the case of $16\text{SbI}_3\text{-}84\text{Sb}_2\text{S}_3$ glass.

Now let us consider what will happen if we start to move the laser spot from the center of a dot to create a line. From Fig. 4(c) it is clear that our laser beam will move from zone S to a “fresh” unilluminated region of glass surface, passing through the P zone. For glass forming composition, for which this zone is a few microns wide, we can expect the presence of additional nuclei within the P zone, especially if we have allowed extensive time for dot growth in zone S . The appearance and growth of dot seed is demonstrated experimentally through an in-situ video recording of laser-induced fabrication of Sb_2S_3 SCAG (dot and following line) on the surface of $16\text{SbI}_3\text{-}84\text{Sb}_2\text{S}_3$ glass (see Video VS1 in Supplementary information). Fig. 5 shows an image sequence received in-situ by a CCD camera for crystal fabrication of Sb_2S_3 crystal on $16\text{SbI}_3\text{-}84\text{Sb}_2\text{S}_3$ glass, shown in Figs. 1 and 2. Within 5 s after starting the irradiation the power density reaches $90 \mu\text{W}/\mu\text{m}^2$ and a light white dot with a $15 \mu\text{m}$ diameter is observed in illuminated area lasting up to 42.9 s. We attribute the slightly white contrast observed initially to diffuse scattering resulting from compositional changes due to SbI_3 evaporation/diffusion. At 43.0 s a sharp increase in the reflected light is observed from the dot area. As indicated in Fig. 5, at this instant the region is found to be crystalline. From this evolution of crystallization we can conclude that the rate of crystal nucleation of the Sb_2S_3 phase is slow. Once a nucleus is formed in the dot center, it grows to $\sim 10 \mu\text{m}$ in ≤ 0.1 s. Taking into account that this Sb_2S_3 dot crystal grows with a high speed of $\geq 100 \mu\text{s}$, we can conclude that once the first nucleus has formed, it grows so fast that there is too little time for the formation of additional nuclei. During the next 22 s the size of the white spot expands slightly (Fig. 5). We duplicate the image received at 65th second of recorded video and mark it with S (area covered by crystal at 43rd second) and expected P zones as well as N region of P zone, as traversed by the laser beam at the beginning of the line scan.

As shown by the EBSD and μ SXRD data presented in Figs. 1 and 2, we observed high angle grain boundaries at exactly the region marked N . Evidently, due to long (65 s) time of dot growth in this region, additional nuclei could form and grow, which only partially aligned to the orientation of the initial crystal growing from the dot and serve as seeds for crystal grains in the line. The additional grains separated by large angle boundaries were observed in about half the experiments, which is a manifestation of the stochastic nature of the nucleation process. Note that the P zone is very narrow for non-glass-forming Sb_2S_3 glass composition and so no additional nuclei appear around the crystal dot in this case. Based on this analysis, we infer that for the laser fabrication of single crystal in glass, a glass-former component (such as SbI_3) may be helpful for making the glass of an otherwise non-glass-forming component (such as Sb_2S_3). However, the addition of too much glass former could help form unwanted nuclei in the vicinity of laser irradiated

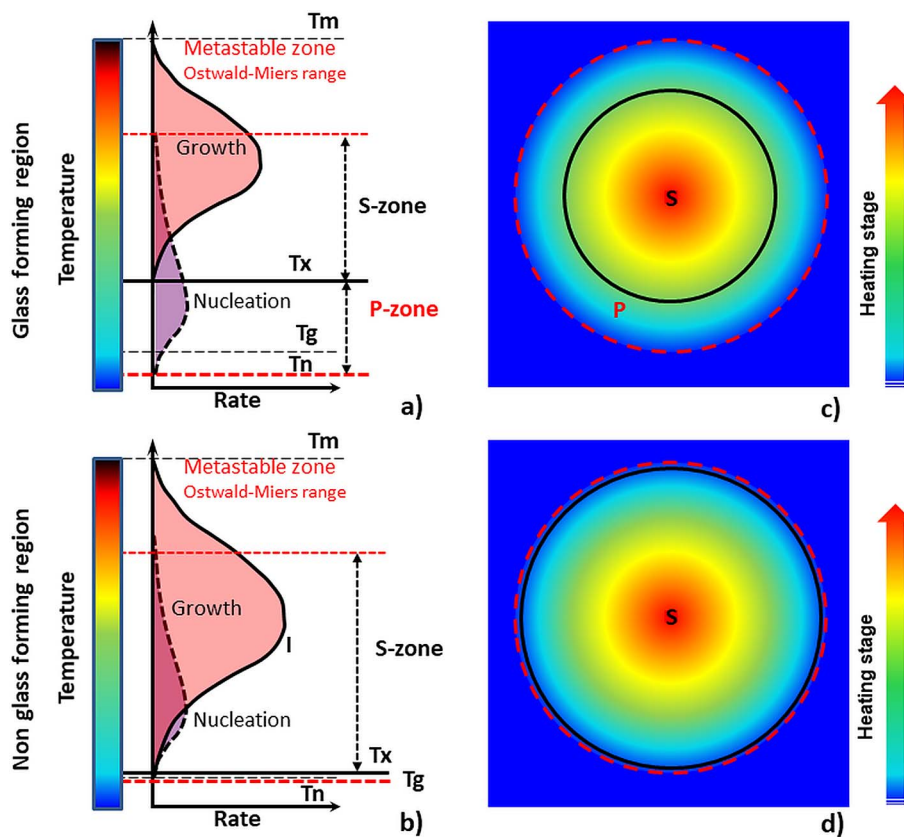


Fig. 4. Temperature dependence of nucleation and crystal growth rates in glass-forming (a, c) and non-glass forming (b, d) systems and its relationship to laser crystallization. Prototypical temperature dependence vs. nucleation and growth rate curves (a, b). Schematic of the CW laser induced temperature fields in the focal spot at the glass surface, with the temperature lines from (a, b) representing the lower limits of nucleation and crystal growth temperature range (c, d). T_m , T_x , T_n and T_g indicate the temperatures of melting, crystal growth onset, nucleation onset and glass transition.

region, which would crystallize subsequently with the displacement of laser.

It should be noted that grain orientation of “the stray” grains in the transition region are not very different from the orientation of the original dot grain. Figs. 1 and 1S (see Supplementary information) show that misorientations of grains in dot, transition region and line do not exceed 10° . It suggests preferential orientation of additional grains forming in this region. One possible explanation is that polarization of laser affects the orientation of nuclei that ultimately become readily observable grains [29–31]. Indeed in our preliminary experiments, we have observed that very often the dots have their $\langle 001 \rangle$ aligned parallel to the plane of laser polarization as well as the glass surface [32]. Secondly, the grains in the transition region appear similar to those formed via non-crystallographic branching (NCB), which is typical of spherulitic growth observed in biominerals and many other materials

[33–44]. In this case, the aligned growth can be explained by a particle attachment model [45], where independently formed ‘particles’, which could be stable nuclei or unstable embryos, try to orient themselves to match the orientation of the crystal at the growth front. Branching or aligned grains form, rather than a perfect single crystal, if this alignment is incomplete. In our case, such particles will form in P region and then attach to the part of single crystal that grows from the dot and follows the laser.

On the surface of $16\text{SbI}_3\text{--}84\text{Sb}_2\text{S}_3$ glass the crystallization of Sb_2S_3 lines is observed at the leading edge of laser heated region (Fig. 5). This fact confirms that the single-crystal Sb_2S_3 line grows during the heating of glass rather than cooling of the melt [9]. Comparatively long time exposures, which are needed for nucleation (few seconds for Sb_2S_3 vs. 30–50 s for $16\text{SbI}_3\text{--}84\text{Sb}_2\text{S}_3$ glasses) confirm that the nucleation rate (probability of nucleation) in laser-heated region - a few microns in size

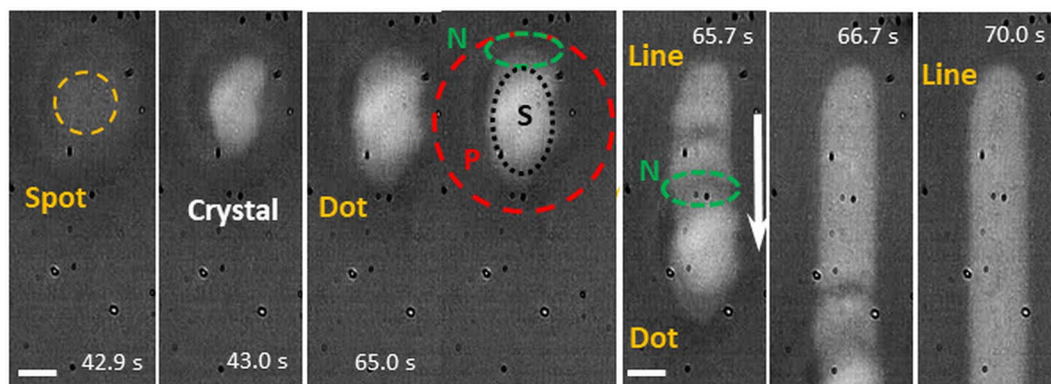


Fig. 5. Optical images collected by CCD camera during laser-induced fabrication of the crystal, which was created by slowly ramping the power density from 0 to $90 \mu\text{W}/\mu\text{m}^2$ (within 5 s), maintaining it for 60 s and then transforming the dot to a crystal line by moving the laser spot at a scanning speed of $20 \mu\text{m}/\text{s}$ on the surface of $16\text{SbI}_3\text{--}84\text{Sb}_2\text{S}_3$ glass. Scale bars correspond to $5 \mu\text{m}$. Numbers on images indicate exposure time from the beginning of irradiation. White arrow shows direction of sample displacement. Small black-white specks in the figure are artifacts of video-recording process, and are unrelated to sample surface.

- of the present glass compositions during *heating* is extremely low relative to the crystal growth rate of Sb_2S_3 phase.

4. Conclusion

We have observed that competition between nucleation and growth of Sb_2S_3 single crystal during laser-induced solid-state transformation of $16\text{SbI}_3\text{--}84\text{Sb}_2\text{S}_3$ glasses often introduces new grains abruptly in the transition region between the crystal dot and line. Such high angle boundaries between the grains are not observed during laser crystallization of Sb_2S_3 glass. This difference in propensity for introducing such defects arises from the difference in their glass-forming ability. For the case of relatively stable non-stoichiometric glass, additional nucleation around the initially formed single crystal dot becomes viable as the growth rate is negligible. Subsequently, these nuclei form unwanted grains as the growth front extends to form the line. So to avoid the appearance of undesirable grains, the addition of glass former should be sufficient to make the glass of otherwise non-glass-forming component. On the other hand, the addition of too much glass former could help form unwanted grains in the vicinity of laser irradiated region. Also once a stable seed has formed, we should move the laser and not allow any further laser heating which would only introduce additional nuclei. Thus, we can minimize the possibility of unwanted nucleation in the 'challenge' zone of transition from dot to line too.

Supplementary data to this article can be found online at <https://doi.org/10.1016/j.jnoncrysol.2017.12.007>.

Acknowledgement

This work was supported by the Basic Energy Sciences Division, Department of Energy (project DE-SC0005010). The Advanced Light Source is supported by the Director, Office of Science, Office of Basic Energy Sciences, Materials Sciences Division, of the U.S. Department of Energy under contract no. DE-AC02-05CH11231 at Lawrence Berkeley National Laboratory and University of California, Berkeley, California.

References

- [1] K. Shinozaki, S. Abe, T. Honma, T. Komatsu, Self-organized homo-epitaxial growth in nonlinear optical $\text{BaAlBO}_3\text{F}_2$ crystal crossing lines patterned by laser in glass, *Opt. Mater.* 49 (2015) 182–189.
- [2] T. Komatsu, T. Honma, Laser patterning and characterization of optical active crystals in glasses, *Asian Ceram. Soc.* 1 (2013) 9–16.
- [3] A. Stone, H. Jain, V. Dierolf, M. Sakakura, Y. Shimotsuma, K. Miura, K. Hirao, J. Lapointe, R. Kashyap, Direct laser-writing of ferroelectric single-crystal waveguide architectures in glass for 3D integrated optics, *Sci. Rep.* 5 (2015) 10391.
- [4] C. Jing, L. Mazerolles, M. Lancry, F. Brisset, B. Pommellec, Modifications in lithium niobium silicate glass by femtosecond laser direct writing: morphology, crystallization, and nanostructure, *JOSA B* 34 (2017) 160–168.
- [5] A. Lipatiev, T. Lipateva, S. Lotarev, A. Okhrimchuk, A. Larkin, M. Presnyakov, V. Sigaev, Direct laser writing of LaBGeO_5 crystal-in-glass waveguide enabling frequency conversion, *Cryst. Growth Des.* 17 (2017) 4670–4675.
- [6] D. Savitskii, H. Jain, N. Tamura, V. Dierolf, Rotating lattice single crystal architecture on the surface of glass, *Sci. Rep.* 6 (2016) 36449, <http://dx.doi.org/10.1038/srep36449>.
- [7] D. Savitskii, H. Jain, C. Au-Yeung, V. Dierolf, N. Tamura, Laser fabrication of 2D rotating-lattice single crystal, *Cryst. Growth Des.* 17 (2017) 1735–1746, <http://dx.doi.org/10.1021/acs.cgd.6b01709>.
- [8] D. Savitskii, H. Jain, C. Au-Yeung, V. Dierolf, N. Tamura, Unpublished results.
- [9] D. Savitskii, B. Knorr, V. Dierolf, H. Jain, Demonstration of single crystal growth via solid-solid transformation of a glass, *Sci. Rep.* 6 (2016) 23324, <http://dx.doi.org/10.1038/srep23324>.
- [10] J. Varghese, S. Barth, L. Keeney, R.W. Whatmore, J.D. Holmes, Nanoscale ferroelectric and piezoelectric properties of Sb_2S_3 nanowire arrays, *Nano Lett.* 12 (2012) 868–872.
- [11] S. Messina, M.T.S. Nair, P.K. Nair, Solar cells with Sb_2S_3 absorber films, *Thin Solid Films* 517 (2009) 2503–2507.
- [12] H. Bao, X. Cui, C.M. Li, Q. Song, Z. Lu, J. Guo, Synthesis and electrical transport properties of single-crystal antimony sulfide nanowires, *J. Phys. Chem. C* 111 (2007) 17131–17135.
- [13] M. Calixto-Rodríguez, H. Martínez, Y. Peña, O. Flores, A. Esparza-Ponce, J. Sánchez-Juárez, J. Campos-Alvarez, P. Reyes, A comparative study of the physical properties of Sb_2S_3 thin films treated with N_2 AC plasma and thermal annealing in N_2 , *Appl. Surf. Sci.* 256 (2010) 2428–2433.
- [14] W. Wisniewski, C.A. Baptista, C. Rüssel, Orientational changes during the surface crystallization of cordierite from a $\text{B}_2\text{O}_3/\text{Al}_2\text{O}_3/\text{MgO}/\text{SiO}_2$ glass, *CrystEngComm* 14 (2012) 5434–5440.
- [15] W. Wisniewski, R. Harizanova, G. Völksch, C. Rüssel, Crystallization of iron containing glass-ceramics and the transformation of hematite to magnetite, *CrystEngComm* 13 (2011) 4025–4031.
- [16] S. Seidel, M. Dittner, W. Wisniewski, W. Höland, C. Rüssel, Effect of the ZrO_2 concentration on the crystallization behavior and the mechanical properties of high-strength $\text{MgO-Al}_2\text{O}_3\text{-SiO}_2$ glass-ceramics, *J. Mater. Sci.* 52 (2017) 1955–1968.
- [17] A.P. Shpak, V.M. Rubish, O.A. Mykaylo, D.I. Kaynts, O.G. Guranich, R.R. Rosul, Optical properties and local structure of $(\text{As}_2\text{S}_3)_{100-x}(\text{SbSI})_x$ glasses Ukr. J. Phys. Opt. 11 (2010) 107–113.
- [18] V. Janošević, M. Mitrić, J. Savić, I. Validžić, Structural, optical, and electrical properties of applied amorphized and polycrystalline Sb_2S_3 thin films, *Metall. Mater. Trans. A* 47 (2016) 1460–1468.
- [19] D. Savitskii, M. Sanders, R. Golovchak, B. Knorr, V. Dierolf, H. Jain, Crystallization of stoichiometric SbSI glass, *J. Am. Ceram. Soc.* 97 (2014) 198–205.
- [20] D. Savitskii, K. Atwater, V. Dierolf, H. Jain, Formation of ferroelectric phases in Sb-S-I glasses, *J. Am. Ceram. Soc.* 97 (2014) 3458–3462.
- [21] M. Kunz, N. Tamura, K. Chen, A.A. MacDowell, R.S. Celestre, M.M. Church, S. Fakra, E.E. Domning, J.M. Glossinger, J.L. Kirschman, G.Y. Morrison, D.W. Plate, B.V. Smith, T. Warwick, V.V. Yashchuk, H.A. Padmore, E. Ustundag, A dedicated superbend X-ray microdiffraction beamline for materials, geo-, and environmental sciences at the advanced light source, *Rev. Sci. Instrum.* 80 (2009) 035108.
- [22] N. Tamura, R. Barabash, G. Ice (Eds.), *Strain and Dislocation Gradients From Diffraction. Spatially Resolved Local Structure and Defects*, Imperial College Press, London, 2014, pp. 125–155 (Chap. 4).
- [23] D. Savitskii, B. Knorr, V. Dierolf, H. Jain, Challenges of CW laser-induced crystallization in a chalcogenide glass, *Opt. Mater. Express* 3 (8) (2013) 1026–1038.
- [24] D. Savitskii, B. Knorr, V. Dierolf, H. Jain, Laser-induced growth of oriented Sb_2S_3 single crystal dots on the surface of $82\text{SbSI-}18\text{Sb}_2\text{S}_3$ glasses, *J. Non-Cryst. Solids* 431 (2015) 36–40.
- [25] I.D. Turyanitsa, T.N. Melnichenko, P.P. Shtets, V.M. Rubish, Glass preparation, structure and properties of alloy in Sb-S-I system, *Izv. AN SSSR: Neorg. Mater.* 22 (1986) 2047–2050 (In Russian).
- [26] A.K. Varshneya, *Fundamentals of Inorganic Glasses*, Academic Press, 1994 (Ch. 3).
- [27] W. Höland, G.H. Beall, *Glass Ceramic Technology*, John Wiley & Sons, Inc., Hoboken, New Jersey, 2012 (Ch. 1).
- [28] E.D. Zanotto, Bright future for glass-ceramics, *Amer. Ceram. Soc. Bull.* 89 (2010) 19–27.
- [29] V. Lyubin, M. Klebanov, Polarization-dependent, laser-induced anisotropic photo-crystallization of some amorphous chalcogenide films, *Appl. Phys. Lett.* 71 (1997) 2118–2120.
- [30] V. Lyubin, M. Klebanov, M. Mitkova, Polarization-dependent laser crystallization of Se-containing amorphous chalcogenide films, *Appl. Surf. Sci.* 154–155 (2000) 135–139.
- [31] K.B. Borisenko, J. Shanmugam, B. Williams, P. Ewart, B. Gholipour, D. Hewak, R. Hussain, T. Javorfi, G. Siligardi, A. Kirkland, Photo-induced optical activity in phase-change memory materials, *Sci. Rep.* 5 (2015) 8770.
- [32] D. Savitskii, C. Au-Yeung, K. J. Veenhuizen, V. Dierolf, H. Jain, Unpublished results.
- [33] A.G. Shtukenberg, Y.O. Punin, E. Gunn, B. Kahr, Spherulites, *Chem. Rev.* 112 (2011) 1805–1838.
- [34] J. L. Hutter, J. Bechhoefer, Banded spherulitic growth in a liquid crystal, *J. Cryst. Growth* 217 (2000) 332–343.
- [35] A.G. Shtukenberg, X. Cui, Jo Freudenthal, E. Gunn, E. Camp, B. Kahr, Twisted mannitol crystals establish homologous growth mechanisms for high-polymer and small-molecule ring-banded spherulites, *J. Am. Chem. Soc.* 134 (2012) 6354–6364.
- [36] D.C. Bassett, On spherulitic growth and cellulation in polymers. A unified context, *Polym. J.* 31 (1999) 759–764.
- [37] X. Wang, R. Liu, M. Wu, Zh. Wang, Yo Huang, Effect of chain disentanglement on melt crystallization behavior of isotactic polypropylene, *Polym.* 50 (2009) 5824–5827.
- [38] Ch.-Yu Sun, M. Marcus, M. Frazier, A. Giuffrè, T. Mass, P.U.P.A. Gilbert, Spherulitic growth of coral skeletons and synthetic aragonite: nature's three-dimensional printing, *ACS Nano* 11 (2017) 6612–6622.
- [39] J. Harris, I. Mey, M. Hajir, M. Mondeshki, S.E. Wolf, Pseudomorphic transformation of amorphous calcium carbonate films follows spherulitic growth mechanisms and can give rise to crystal lattice tilting, *CrystEngComm* 17 (2015) 6831–6837.
- [40] F. Arzilli, L. Mancini, M. Voltolini, M.R. Cicconi, S. Mohammadi, G. Giuli, D. Mainprice, E. Paris, F. Barou, M.R. Carroll, Near-liquidus growth of feldspar spherulites in trachytic melts: 3D morphologies and implications in crystallization mechanisms, *Lithos* 216–217 (2015) 93–105.
- [41] G. Ryschenkow, G. Faivre, Bulk crystallization of liquid selenium. Primary nucleation, growth kinetics and modes of crystallization, *J. Cryst. Growth* 87 (1988) 221–235.
- [42] I.E. Bolotov, A.V. Kozhin, S.B. Fischeleva, Branching-induced formation of spherulites in In_2Se and Sb_2Se_3 films, *Sov. Phys. Crystallogr.* 15 (1970) 461–464.
- [43] V.M. Kosevich, A.A. Sokol, A.G. Bagmut, Structure of Sb_2S_3 spherulite crystals studied by crystal lattice images, *Sov. Phys. Crystallogr.* 24 (1979) 80–83.
- [44] A.G. Bagmut, S.N. Grigorov, V.Y. Kolosov, V.M. Kosevich, G.P. Nikolaychuk, The growth of Sb_2S_3 crystals with bend lattice during amorphous films annealing and condensation, *Funct. Mater.* 12 (2005) 461–466.
- [45] J.J. De Yoreo, P.U.P.A. Gilbert, N.A.J.M. Sommerdijk, R. Lee Penn, S. Whitelam, D. Joester, H. Zhang, J.D. Rimer, A. Navrotsky, J.F. Banfield, A.F. Wallace, F. Marc Michel, F.C. Meldrum, H. Cölfen, P.M. Dove, Crystallization by particle attachment in synthetic, biogenic, and geologic environments, *Science* 349 (2015) aaa6760.